Journal of
Materials Chemistry C

Materials for optical, magnetic and electronic devices

Accepted Manuscript

This article can be cited before page numbers have been issued, to do this please use: X. Guo, B. Yang, X. Zhang, J. Lu, M. Huang, N. Huang, L. Liu and X. Jiang, *J. Mater. Chem. C*, 2024, DOI: 10.1039/D4TC02335H.

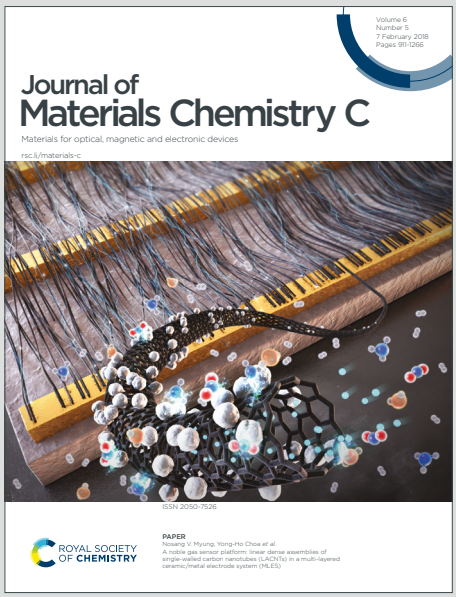

ROYAL SOCIETY OF CHEMISTRY

rsc.li/materials-c

View Article Online
DOI: 10.1039/D4TC02335H

ARTICLE

Diamond photo-electric detectors with introducing silicon-vacancy color centers

Received 00th January 20xx,
Accepted 00th January 20xx

DOI: 10.1039/x0xx00000x

Xiaokun Guo,[a,b] Bing Yang,*[a,b] Xinglai Zhang,[a,b] Jiaqi Lu,[a,b] Ming Huang,[a,c] Nan Huang,[a,b] Lusheng Liu[a,b] and Xin Jiang,*[d]

Color centers in diamond is a type of promising candidate for quantum sensing under photo-luminescent or photo-electric mode. Photoinduced charge carrier separation for nitrogen-vacancy (NV) centers makes diamond an excellent visible photodetector. To date, the introduction of silicon-vacancy (SiV) color centers on the photo-electrical and photo-luminescent properties of diamond remains unclear. To address this issue, high-quality silicon-doped single crystal diamond (Si-SCD) photodetectors were prepared by microwave plasma chemical vapor deposition (MPCVD). It is found that an extremely low dark current of several picoampere can be achieved with an oxygen-terminated surface. In addition, although the introduction of SiV centers enhances the device's absorption of near-ultraviolet/visible (NUV/Vis) illumination, it has little impact on the solar blind detection performance, exhibiting a responsivity of 36.2 mA/W and detectivity of 2.10×10^{12} Jones. Meanwhile, the Si-doped detector also exhibits 10^2 to 10^3 times higher responses to NUV/Vis signals and a faster cut-off speed. Moreover, a SiV PL enhancement of 50% was achieved at external electrical bias, which shows a higher electric pumping efficiency compared with polycrystalline diamond devices.

1. Introduction

Diamond photodetectors have received considerable attention during the past decades owing to their excellent physical properties such as wide band gap (5.47 eV), high breakdown voltage (10^7 V·cm^{-1}), carrier mobility (2200 cm^2·V^{-1}·s^{-1}), high thermal conductivity and radiation resistance. [1-5] This makes it work in solar-blind wavelength (< 280 nm) with high detection accuracy and low false-alarm rate. To optimize the performance of diamond UV detectors, much effort has been made on the device geometries such as metal-semiconductor-metal structure with Ohmic or Schottky contact and p-n junctions. [6,7] The crystallinity of diamond will also affect the photo-electrical signals of the device. Recent studies show polycrystalline diamond films with high-crystalline quality could also exhibit a high response to UV signals. [8,9]

Color centers, such as nitrogen-vacancy (NV) and silicon-vacancy (SiV), are one type of optically active point defects in diamonds. They exhibit outstanding optical properties such as strong fluorescent emission at visible and near-infrared wavelengths at room temperature, optical initialization and read out by microwave or laser, and perfect photo-stability without photo-bleaching or photo-blinking, which can be applied in the area of quantum information processing, quantum sensing and biological marking. [10-13] Traditionally, the readout of color centers was realized by photoluminescence (PL) using confocal microscopy. Recently, it was reported that the photoinduced current signals with microwave frequencies and magnetic fields exhibited similar variation with that of optical signals for NV centers present in type Ib single-crystalline diamonds. [14-17] It implied the readout of the electron spin state of NV centers could be realized by photoelectric detection. Sittimart et al.[14] fabricated a visible photo-electrical detector with high thermal stability and radiation resistance using NV centers owing to its deep state in bandgap. A two-photon absorption model with charge carriers excited to the conduction band of diamond and collected by electrode was proposed to explain the generation of electrical signals at external bias. Different from NV centers, SiV centers in diamond exhibit a narrower and stronger zero phonon line centered at 738 nm with weak electron-phonon coupling, which may be beneficial for photoinduced carrier transport. [18-20] However, because the atomic radius of Si is much larger than that of N and C, incorporation of Si atoms into diamond lattice will lead to increased local stress although their concentration is much lower, which may deteriorate their photo-electric performance. In such cases, the photoinduced carrier separation and recombination will be complex for SiV centers. The effect of the introduction of SiV centers on the photo-electric response of diamonds remains unclear.

In this work, the effects of SiV centers on the optical and electrical properties of photodetectors are studied. A Si-doped epitaxial layer is deposited on a high-quality single-crystal diamond (SCD) substrate for the introduction of SiV centers. Raman spectra confirm that Si-doped diamonds (Si-SCD) exhibit good crystalline

[a] Shenyang National Laboratory for Materials Science, Institute of Metal Research (IMR), Chinese Academy of Sciences (CAS), No. 72 Wenhua Road, Shenyang, 110016, China.
[b] School of Materials Science and Engineering, University of Science and Technology of China, No. 72 Wenhua Road, Shenyang 110016, China.
[c] School of Environment and Chemical Engineering, Shenyang University of Technology, Shenliao West Road 111, Economic & Technological Development Zone 110870 Shenyang, China.
[d] Institute of Materials Engineering, University of Siegen, Paul-Bonatz-Str. 9-11, Siegen, 57076, Germany.

quality. Compared with the undoped substrate, the Si-SCD exhibits a similar response and detectivity in the wavelength of 220 nm along with a remarkable photocurrent generated in the visible light. Moreover, an obvious PL enhancement can be detected with bias voltages applied, which shows a higher quantum efficiency compared to polycrystalline diamond-based heterostructure. These phenomena provide feasible approaches to realize the functionalize of diamond photodetectors.

2. Experimental section

The Si-SCD membrane was homoepitaxially deposited on commercially available type-Ib single crystalline diamond (SCD) substrate with a size of 5 ×5 ×0.3 mm using an MPCVD technique. Firstly, the SCD substrate was boiled with mixed acid (H_2SO_4: HNO_3 = 3:1) at 200 ºC for 2 h to remove nitrogen and other impurities, followed by supersonically washing with acetone, ethanol and deionized water for 20 min, respectively. The reactive gas source was a mixture of methane and hydrogen with a gas flow rate of 300 and 18 sccm, respectively. The tetramethylsilane (TMS, 1.15 wt% diluted in hydrogen) was added with a flow rate of 1 sccm for the in-situ formation of SiV centers. [21,22] Other growth parameters were as follows: microwave power of 6 kW, chamber pressure of 36 mbar, substrate temperature of about 660 ºC and deposition duration of 8 h. After deposition, both the Ib SCD sample (defined as undoped SCD as a control group) and the Si-SCD sample were cleaned again with the mixed acid to remove the surface contamination that may be introduced by CVD process. Surface terminations of hydrogen and oxygen were introduced by hydrogen plasma treatment and annealing in air both at 600ºC for 30 min, respectively.[23,24]

The microstructures and optical properties of the undoped SCD and Si-SCD diamond films were characterized by field-emission scanning electron microscopy (FE-SEM, Hitachi SU-70), transmission electron microscopy (TEM, FEI Tecnai G2 F20), Raman spectrometer (LabRAM HR Evolution, Horiba, 532 nm excitation laser), ultraviolet-visible absorption spectrum (UV-Vis, Hitachi U-3900). The optoelectronic performances of devices were measured using a semiconductor characterization system (SCS, KEITHLEY 4200) equipped with a probe station and multiple light sources (LEDs and Xe lamp). The Ti/Au (30nm/30nm) interdigital electrodes with a space of 10 μm were patterned and prepared by UV lithography and electron beam evaporation (EBE) processes (shown as Fig. 1(b)). Annealing in argon atmosphere at 700 ºC for 3 min was conducted to make Ohmic contact for the electrode. [25] The schematic of the device (with probe station and light source) is shown in Fig. 1(a). The electrically pumped PL spectra were recorded using Raman spectrometer with 50 × objective (numerical aperture of 0.5) at different bias voltages.

3. Results and discussion

Fig. 2(a) shows planer optical and SEM images of the as-deposited Si-SCD samples, a flat and smooth crystal surface without any macroscopic defects can be observed. The epitaxial Si-SCD film with identical deposition parameters for 30 min is used to prepare the cross-section TEM sample for characterization of the growth rate and crystalline quality of the samples with long deposition duration, as shown in Fig. 2 (b). The epitaxial film of approximately 230 nm in thickness reveals a relatively low growth rate of 460 nm per hour, which is important for ensuring high crystal quality. [21] It is estimated that the film deposited for 8h exhibits a thickness of about 3.68 μm. No crystalline defects such as dislocation or twin are observed in the films. The diffraction spots shown in the inset of the selected area electron diffraction (SAED) pattern indicate a single crystalline nature with two characteristic crystal plane families of {220} and {400}. However, some lattice defects are observed to be located at the interface between the substrate and the epi-layer, as marked by the yellow circles. Their presence may affect the impurity distribution and optical properties of the sample. The AFM measurement in Fig. S1(a) in supplementary materials reveals that the surface RMS roughness of the Si-SCD sample is 1.52 nm, close to the undoped SCD substrate. From the Raman spectra (Fig. 2(c)), the Si-SCD exhibits a strong peak centered at 1332.8 cm^{-1}, corresponding to the first-order Raman line of diamond. The absence of characteristic peaks of sp^2-D (1350 cm^{-1}), sp^2-G (1580 cm^{-1}) and trans-polyacetylene (TPA, 1510 cm^{-1}) indicates high crystalline quality of the Si-doped SCD sample. [26,27] Moreover, the full width at half maximum (FWHM) of the diamond Raman peak is estimated to be 2.82 cm^{-1}, which is slightly larger than that of the undoped SCD substrate (2.70 cm^{-1}). Such value is smaller than that of the polycrystalline diamond films (≈5 cm^{-1}) deposited with a lower methane ratio, [28] and similar to the value of CVD epitaxial single crystal diamond (FWHM≈2.8 cm^{-1}) reported previously. [29] This

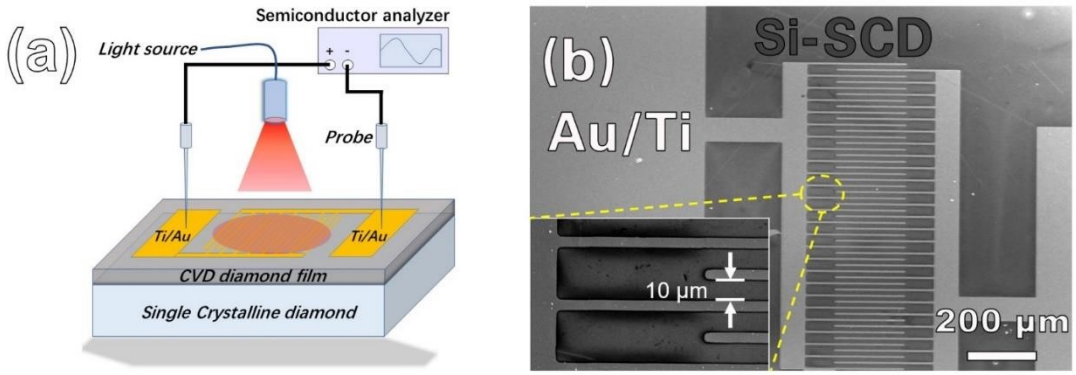

Fig. 1 Schematic diagram (a) and SEM image (b) of the Si-doped SCD photodetector with planar interdigital electrodes.

View Article Online
DOI: 10.1039/D4TC02336H

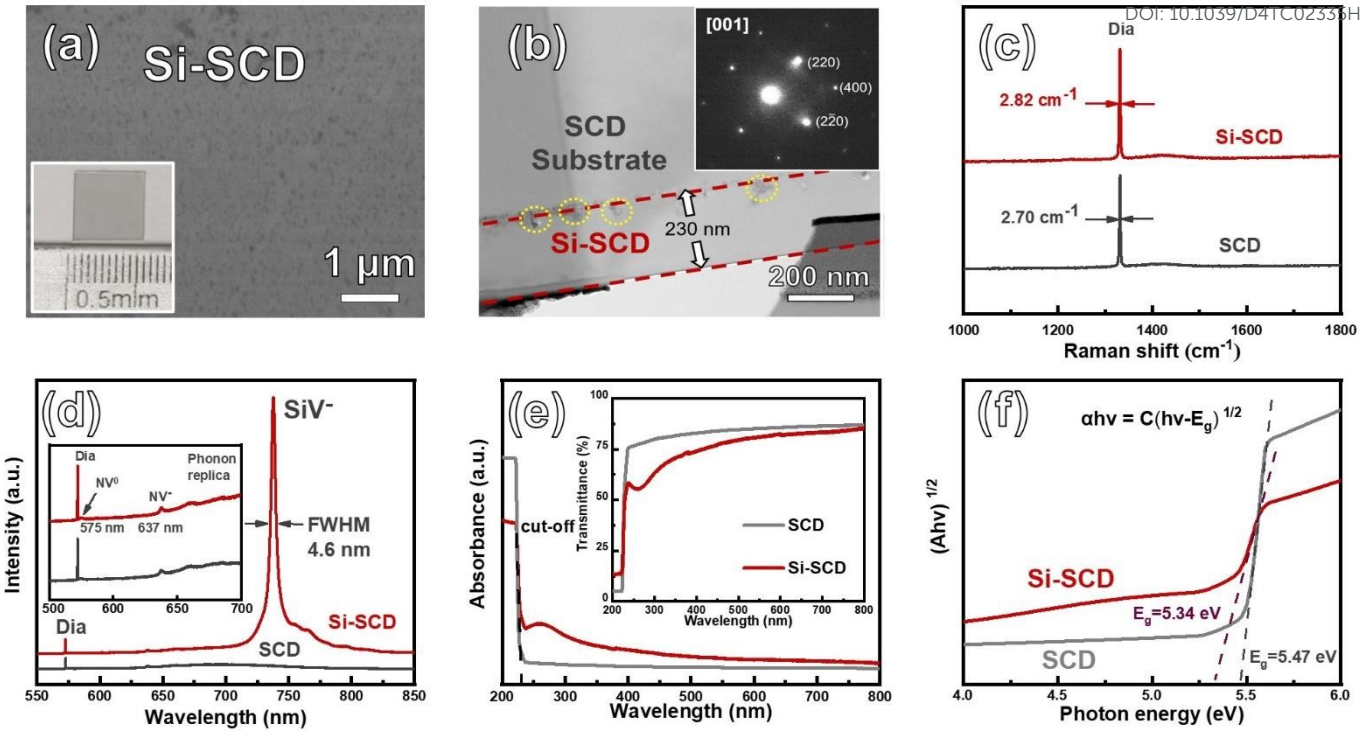

Fig. 2 Plan-view SEM image (a) and TEM cross-section image (b) of the Si-doped SCD sample. Room temperature Raman spectra (c), PL spectra (d), UV-Vis absorption/transmittance spectra (e) and the corresponding Tauc plot (f) of the samples.

implies that the diamond phase is crystallized in good quality in the Si-doped SCD sample. No severe deterioration in the crystal quality of the single crystalline diamond is crucial for high-performance optoelectronic devices.

The room temperature PL spectrum of the Si-doped SCD sample is demonstrated in Fig. 2(d). Compared to the SCD sample, the Si-doped SCD sample shows a sharp peak centered at 738 nm along with a sideband at 757 nm, which are assigned to be zero phonon line (ZPL) and phonon replica of negatively charged SiV^- centers. [30] It is noted that the SiV peak intensity is about 10 times higher than that of the diamond Raman peak (572.6 nm), This suggests that Si atoms are successfully doped into the epitaxial layer of SCD and participated in the formation of high-brightness SiV centers. The FWHM of the SiV^- ZPL is estimated to be about 4.6 nm according to the peak de-convolution procedure using Gauss-Lorentz fitting, similar to that of the reported single-crystal diamond (4.5 ~ 5.4 nm). [31] This means that small local stress is generated in the Si-SCD epitaxial layer. One explanation is the introduction of Si atoms in diamond lattice does not give rise to remarkable internal stress compared to that induced by the mismatch in lattice constant and thermal expansion for hetero-grown diamond films on foreign substrates. [32] In addition, an NV^0 peak centered at 575 nm and an NV^- peak centered at 637 nm is also observed in the Si-doped SCD sample (the inset in Fig. 2(d)). [33]

According to the UV-Vis absorption spectra shown in Fig. 2(e), the Si-doped SCD sample shows a UV cut-off edge at 227 nm with a wide absorption band from the UV to the visible region. In contrast, the SCD sample has an increased intrinsic absorption with a lower absorption band in the visible range. Considering that the Si-doped SCD sample has high crystal quality without macroscopic defects, the visible absorption band may be caused by the introduction of SiV and NV centers. Correspondingly, the transmittance curves of the inset (Fig. 2(e)) show a lower transparency at the visible region for the Si-doped SCD sample compared to the SCD sample. Moreover, the bandgap (E_g) can be fitted by the Tauc equation:

$$(\alpha h\upsilon)^n = C(h\upsilon - E_g)$$

Where the $h\upsilon$ and α are the incident photon energy and the absorption coefficient, the C is the proportionality constant. The value of n is 0.5 and 2 for semiconductors with direct and indirect bandgap, respectively. The result (Fig. 2(f)) shows the E_g of the Si-doped SCD sample is 5.36 eV, lower than the undoped substrate (5.47 eV). The narrower E_g of Si-SCD is attributed to the Si doping induced shallow defects that contribute to the absorption below the bandgap. [34]

Generally, low dark current is very favorable for the performance of the photodetector, [35,36] and this current can be effectively tuned by surface termination of diamond. Fig. 3(a) shows the dark current (I_D) of the photodetectors for Si-SCD after different surface terminal modifications. It is noted that the H-terminated SCD (H-SCD) exhibits the highest I_D value of about 92.5 mA at 15 V bias voltage. Considering that the effective area between the interdigital electrodes is about 0.003 cm^2, the calculated surface resistivity is about 5.41×10^4 $\Omega\cdot cm^{-2}$. The high conductivity of H-SCD may be attributed to its two-dimensional hole gas (2-DHG) on the surface acting as a conductive channel. [37] When the treatments of acid oxidation (black curve) and annealing in the air (red curve) were

View Article Online
DOI: 10.1039/D4TC02335H

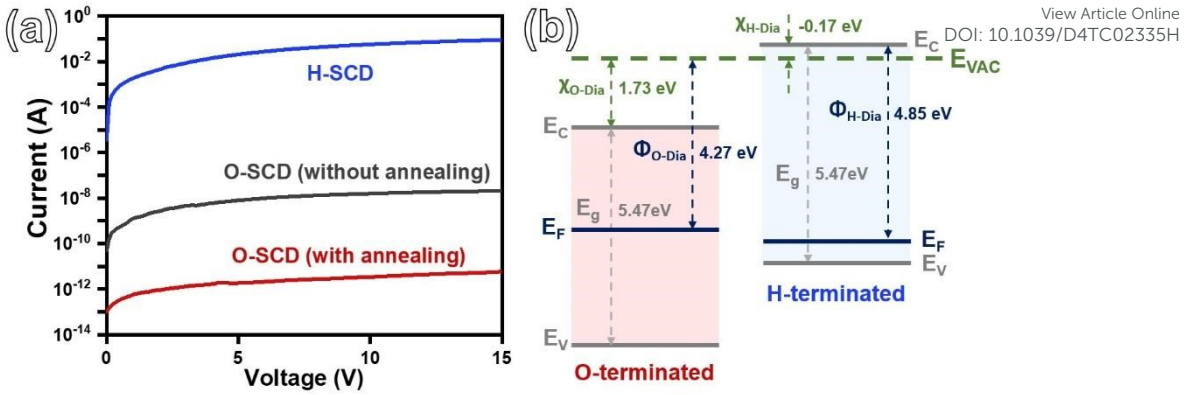

Fig. 3 (a) Dark current of the Si-doped SCD sample with different surface terminals (the grey curve represents the original Si-doped simple with weak oxygen terminal without air annealing). (b) The energy band structures of the diamond terminated with oxygen and hydrogen.

conducted sequentially, the dark currents for the O-terminated SCD (O-SCD) samples decreased significantly. It is only about 5.66×10^{-12} A in the air annealed sample, nearly 10^{10} times lower than the H-SCD. The surface resistivity is calculated to be $R \approx 8.83\times 10^{14}$ $\Omega \cdot cm^{-2}$. The variation in surface conductivity with different surface terminations is caused by the variation in carrier concentration.[38] The effect of surface modification on carrier concentration is explained by energy band structure (Fig. 3(b)), where the work functions and the electron affinities can be determined using Kelvin probe force microscope (KPFM) and ultraviolet photoelectron spectroscopy (UPS) techniques, as shown in Fig. S1 and Fig. S2 in supplementary materials. The work functions of the H-SCD and O-SCD samples are measured to be 4.85 and 4.27 eV, respectively. The H-SCD sample exhibits a negative electron affinity, which is much smaller than the positive electron affinity for the O-SCD sample. As a result, the Fermi level is located close to the valence band for the H-SCD sample, corresponding to p-type conductivity at the surface of H-SCD, which provides a high concentration of hole for surface conductivity. In comparison, the air-annealed O-SCD sample exhibits a nearly intrinsic conductivity at the surface. Therefore, to obtain high performance of the photodetector, photoelectric measurement is conducted on the oxygen-terminated diamond treated by air annealing in the following section.

The photocurrent (I_{Ph}) of the Si-doped diamond sample with oxygen termination was measured under light illumination of different wavelengths, as shown in the multicolor curves in Fig. 4(a) and 4(b). The photocurrent of the Si-doped diamond sample is increased with the bias and reaches saturation at 15 V for all the wavelengths. An extremely high saturation I_{Ph} of 3.58×10^{-8} A was generated at a UV wavelength of 220 nm, which is attributed to its stronger absorption of intrinsic excitation below 227 nm. Such a value is slightly lower than the intrinsic excitation of the undoped

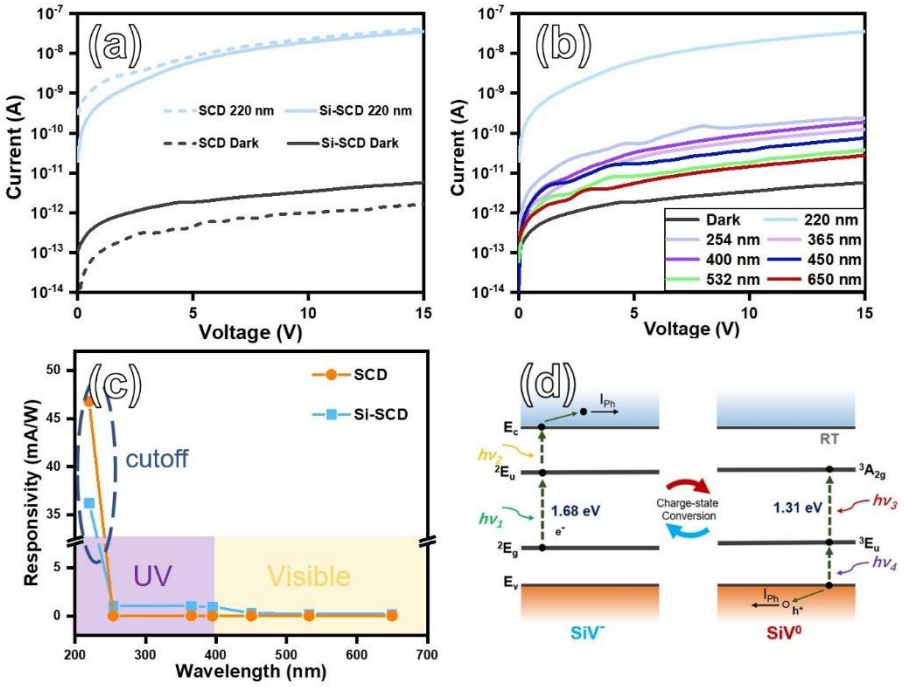

Fig. 4 (a) Dark currents (grey curves) and 220nm intrinsic photocurrents (blue curves) of the SCD and Si-SCD devices. (b) Photocurrent of the Si-SCD device (colored curves) at illuminations of different wavelengths. (c) The device's responsivities to light illumination of different wavelengths. (d) Schematic of carrier transport during the photoionization processes of SiV centers.

View Article Online
DOI: 10.1039/D4TC02335H

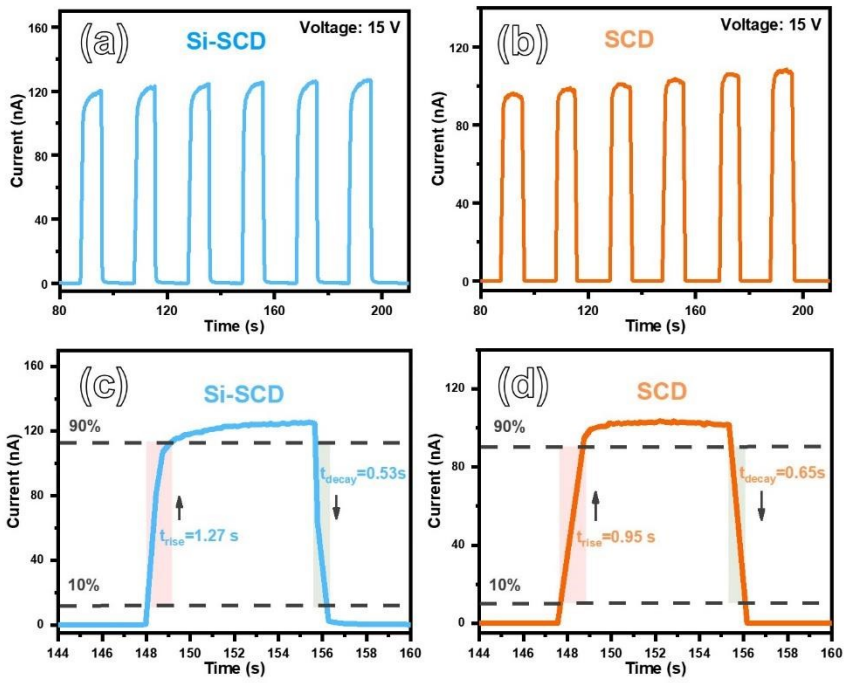

Fig. 5 Time-resolved photocurrent of the Si-doped (a and c) and the undoped (b and d) SCD detectors.

SCD sample (4.63×10^{-8} A). This implies that the introduction of SiV centers does not lead to a severe deterioration in device response to solar blind signals. The optical on-off ratio (I_{Ph}/I_D) of the Si-doped diamond device at 15V bias is calculated to be approximately 6.33×10^{3}, which is about one-quarter the ratio of the SCD (2.92×10^{4}). In addition, it is observed that the I_{Ph} of the Si-doped diamond device under different near-ultraviolet (254 nm, 365 nm) and visible (400 nm, 450nm, 532nm, 650 nm) irradiations are smaller than the intrinsic excitation under 220 nm. However, the I_{Ph} at the above-mentioned light sources for the Si-doped diamond device is larger than that for the undoped substrate, which is caused by its wide absorption band from 250 to 800 nm (red curve in Fig. 2(d)). To further evaluate the device performance, their responsivities (R) to light of different wavelengths are calculated according to the following equation:

$$R_\lambda = \frac{I_{net}}{P \cdot S} = \frac{I_{Ph} - I_D}{P \cdot S}$$

Where the I_{net} represents the net photocurrent and equals the photocurrent (I_{Ph}) minus the dark current (I_D), the S is the irradiation area (0.003 cm^2), and the P is the optical power density of light sources (Tab. S1). The calculated responsivities of the Si-doped diamond device are shown in Fig. 4(c). The responsivity of the Si-doped diamond device under 220 nm irradiation (R_{220}) is 36.2 mA/W, which is slightly lower than the SCD (46.8 mA/W). Therefore, the solar blind detection performance of Si-doped diamond is not seriously deteriorated. Under the NUV-Vis irradiations (Tab. S2), the Si-SCD shows stronger responsivity (10^{-5} ~ 10^{-3} A/W) than the SCD (10^{-7} ~ 10^{-5} A/W). This can be explained by the photoionization of color centers, [39] which mainly involves the excitation and transition processes of carriers at defect levels of SiV centers, as shown in Fig. 4(d). Because the electron-phonon coupling of SiV under room temperature (300 K) is weak and the spin-orbit interaction is strong, its ground state level and excited state level are both doubly degenerate or singlet states. [40] When the excitation light is illuminated, the electrons at ^2E_g double ground state of SiV^- can be excited to the ^2E_u double excited state by one photon. Then, the electron undergoes a photoionized transition to the diamond conduction band (CB) by absorbing the second photon, turns to a free electron and generating a photocurrent, which also leads to the transformation of SiV centers from negative (SiV^-) to neutrality (SiV^0). Similarly, as for SiV^0 centers, an electron can be excited from the ^3E_u ground state to the $^3A_{2g}$ excited state, leaving a hole on the ground state level and subsequently being filled by a transited electron of the valence band (VB). This process can generate a free hole in VB and cause the transition from SiV^0 to SiV^-. As a result, a stronger re sponse to NUV-Vis illumination could occur by the photoionization mechanism of SiV centers.

The UV/Visible rejection ratio (R_{220}/R_{400}) and detectivity ($D^*=R_{220}/\sqrt{2q\times J_D}$) are calculated to evaluate optical selectivity and sensitivity of the devices. Here, R_{220} and R_{400} are the responsibilities of the devices under 220 nm and 400 nm illuminations, respectively. The q is elementary charge equals 1.6×10^{-19} C, the J_D is the dark current density. The results are shown in Tab. 1. The rejection ratio of the Si-SCD device is estimated to be 140, which is much lower than that of the undoped diamond device (78400). However, the detectivity of the Si-doped SCD device is estimated to be 2.10×10^{12} Jones, which is slightly lower than that of the undoped diamond device (5.26×10^{12} Jones). This value is close to that of an all-carbon diamond photodetector using graphite interdigital electrodes ($D^*=1.39\times10^{12}$ Jones), [41] but much higher than the D^* of detector based on TiO_2/Diamond heterostructure ($D^*=6.57\times10^{10}$ Jones). [42] The above results show that the planar Si-doped diamond photodetectors prepared in this work demonstrate high detection rates for deep UV wavelength.

View Article Online
DOI: 10.1039/D4TC02335H

Tab. 1 Comparison of device parameters in this work with previous reports.

Device	I_D (A)	On-off ratio	R (mA/W)	R_{UV}/R_{Vis}	D* (Jones)	t_{rise}/t_{decay} (sec)	Reference
Si-SCD	**5.66×10^{-12}**	**6.33×10^{3}**	**36.2**	**140**	**2.10×10^{12}**	**1.27/0.53**	**In this work**
SCD	1.1×10^{-12}	1×10^{4}	48.0	1×10^{4}	---	~80/---	[29]
SCD	3.68×10^{-13}	20.8	7.86	~50	---	---	[46]
B-SCD/Al	1.0×10^{-12}	~10	28.0	1×10^{3}	---	---	[47]
SCD/TiO_2	1.12×10^{-12}	6.7×10^{7}	200	1×10^{5}	6.57×10^{10}	$2\times10^{-5}/1\times10^{-3}$	[42]
SCD/Gr	5×10^{-6}	~120	21800	8.9×10^{3}	1.39×10^{12}	$3.1\times10^{-4}/3.3\times10^{-4}$	[41]

Fig. 5(a)-(d) shows the time-resolved photocurrent of the devices under 15 V bias and 220 nm illumination. It can be seen that the current of the two devices can be reversibly modulated with light illumination (Fig. 5(a) and 5(b)), exhibiting high stability and repeatability, which is crucial for applications in communication systems. [43] The rise (t_{rise}) and drop (t_{decay}) periods of I_{Ph} is generally defined as the response time required for the photocurrent changing from 10% to 90% of the maximum value. Accordingly, the t_{rise} of the undoped and the Si-SCD devices are estimated to be 0.95 sec and 1.27 sec, respectively. This implies that the introduction of Si dopant prolongs the t_{rise} by about 1/3. The time resolved photoluminescence (TRPL) measurement (Fig. S3) has been applied to study the lifetime of photoinduced carriers in both samples, the average lifetime of the Si-SCD and the SCD is 3.80 and 4.50 ns, respectively. This indicates a higher defect density in Si-doped sample that may lead to a trapping effect and prolong the response time of photocurrent. On the other hand, the corresponding t_{decay} of the two devices is 0.65 sec and 0.53 sec (Fig. 5(c) and 5(d)), implying a shorter lifetime of non-equilibrium carriers. The Si-doped SCD devices exhibit a faster response during the photocurrent drop stage, suggesting that the carriers in the Si-SCD detector recombine more rapidly upon the shutdown of light illumination. Generally, the shorter lifetime usually derives from Shockley-Read-Hall (SRH) recombination, [44] while the longer lifetime could be attributed to the de-trapping of carriers at defects. [45] In our work, it is believed that the existence of SiV defects further promotes carrier recombination and reduces the drop time, which is beneficial for achieving a fast cut-off of photodetectors. A comparison with the reported parameters of diamond-based photodetectors is listed in Tab. 1. Our devices exhibit relatively high detectivity to solar blind signals as well as an ideal on-off ratio compared to most of the devices reported previously. [29,41,42,46,47] Hence, for single crystal diamond photodetectors, the introduction of SiV centers does not lead to a significant deterioration of its intrinsic performance, meanwhile, promotes its response to near-ultraviolent and visible signals.

In addition to the inflorescent SRH recombination, fluorescent recombination of charge carriers also occurs during their separation at external bias, which will vary the PL emission of color centers. The electrically pumped PL spectra of SiV centers were recorded at the diamond region close to the electrode using a Raman spectrometer (532 nm laser) with a high-precision DC power supply, as shown in Fig. 6(a). For a clearer comparison, the results are normalized by the diamond Raman peak at 572.6 nm. The inset shows the CCD optical image during testing with the laser spot size of approximately 1 μm ($d=1.22\lambda/N_A$), which is much smaller than the interdigital electrode spacing (10 μm). The results show that the PL of SiV^- (738 nm) significantly increases with bias voltage, namely, the radiative recombination of injected carriers occurs at SiV defects and enhances its PL emission. This is consistent with our previous work, [48] where a similar PL variation also appears for polycrystalline diamond/heavy-doped n-type Si vertical heterostructure (Dia/n^+-Si) under the electrical pump. Fig. 6(b) shows the normalized PL intensity of the Si-doped SCD device. It can be seen that the PL of the Si-SCD device increases by 50% at 60 V bias, which is slower than the PL enhancement for the Dia/n^+-Si heterostructure (90% at 50 V), owing to the higher injection current for forward-biased diode and wider tailoring region for vertical structure. For further evaluation, the electrical enhancement

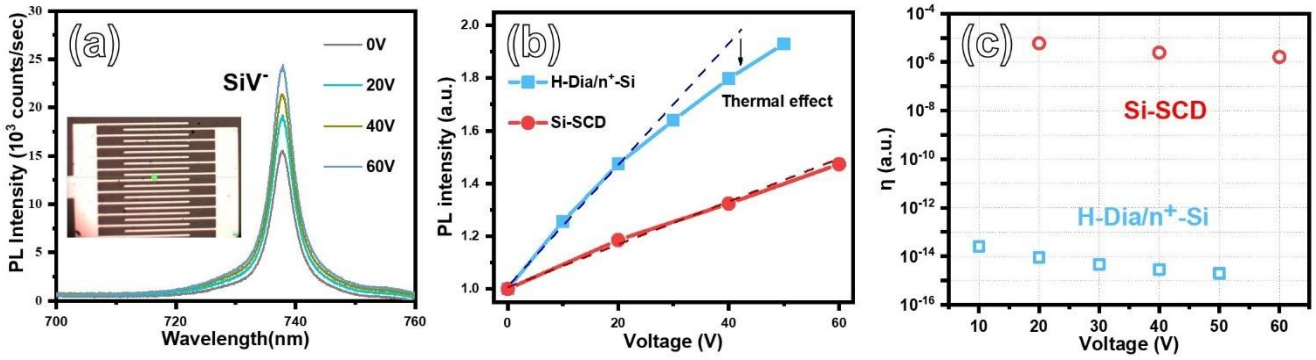

Fig. 6 (a) PL spectra (532 nm laser) of the Si-doped SCD device at different bias voltages. The Normalized SiV^- PL variation (b) and the calculated electrical enhancement efficiency at different bias voltages (c).

efficiency (η) is defined as the power of the net number of emitted photons divided by the power of injected carriers, shown in the equation below:

$$\eta = \frac{P_{Photon(net)}}{P_{Electric}} = \frac{\Delta n_{Ph} \cdot (hc/\lambda)}{I \cdot V}$$

Here, the Δn_{Ph} is the net number of electrically generated photons (PL counts with bias minus PL counts at 0V), the h is the Plank constant, the c is light velocity, the λ is 738 nm for SiV^- photons, the V and the I are applied bias and injected current, respectively. From the calculation results demonstrated in Fig. 6(c), the η of the Si-SCD is about 10^9 times higher than that of the diamond heterostructure, indicating that the device in this work has higher efficiency for radiative recombination, which is crucial for the application in high performance electric-pumping SiV single-photon emitter. There are fewer crystalline defects generated in the single-crystalline diamond films, which reduces the non-radiative process (decreasing the non-linearity of PL in Fig. 6(b)) and enhances the PL emission of SiV centers. Therefore, the high quality of single-crystalline diamond contributes to high electric pumping efficiency for SiV optical emission.

4. Conclusions

In this work, high quality silicon-doped single crystal diamond photodetector was prepared by MPCVD and photolithography techniques. High-brightness SiV centers are introduced with slightly deteriorating the crystal quality. The Si-doped photodetector with oxygen termination exhibits a responsivity of 36.2 mA/W with the detectivities of 2.10×10^{12} Jones at 220 nm illumination, implying that the introduction of the SiV centers will not significantly reduce the intrinsic response of diamond. Owing to the SiV center, the Si-doped photodetector exhibits a near-UV/visible responsivity of 10^2 to 10^3 times higher than that of the undoped photodetector. Additionally, a faster cut-off speed is realized for the Si-doped photodetector, which is attributed to the photoionization of SiV defects and the SRH recombination of photogenerated carriers. In addition, a 50% PL enhancement of SiV centers was achieved for the Si-doped photodetector by applying an external electrical field, which originates from the radiative combination of photo-induced charge carriers. The single-crystalline diamond device exhibits 10^9 times electrical enhancement efficiency for SiV PL emission compared to the polycrystalline diamond devices, making it also a potential candidate in the application of room temperature single photon source.

Author contributions

Xiaokun Guo: Conceptualization, Data curation, Formal analysis, Investigation, Methodology, Visualization, Validation, Writing-original draft and Writing-review & editing. **Bing Yang:** Conceptualization, Formal analysis, Funding acquisition, Project administration, Resources, Supervision and Writing-review & editing. **Xinglai Zhang**: Formal analysis, Resources and Methodology. **Jiaqi Lu:** Data curation, Formal analysis and Methodology. **Ming Huang:** Data curation, Formal analysis and Resources. **Nan Huang:** Project administration and Resources. **Lusheng Liu:** Resources and Supervision. **Xin Jiang:** Funding acquisition, Project administration, Resources and Supervision.

Conflicts of interest

There are no conflicts to declare.

Data availability

The data supporting this article have been included as part of the Supplementary Information.

Acknowledgements

B.Y. would like to thank the National Natural Science Foundation of China (Grants No. 52172056) and the National Natural Science Foundation from Liaoning province (No. 2022MS009) for financial support.

Notes and references

1 Y. Lu, C. Lin and C. Shan, *Adv. Opt. Mater.*, 2018, **6**, 1800359.
2 C. Xie, X. Lu, X. Tong, Z. Zhang, F. Liang, L. Liang, L. Luo and Y. Wu, *Adv. Funct. Mater.*, 2019, **29**, 1806006.
3 H. Chen, H. Liu, Z. Zhang, K. Hu and X. Fang, *Adv. Mater.*, 2016, **28**, 403-433.
4 Z. Zhang, C. Lin, X. Yang, J. Zang, K. Li, Y. Lu, Y. Li, L. Dong and C. Shan, *J. Mater. Chem. C*, 2022, **10**, 6488-6496.
5 U. F. Ahmad, Y. S. Wudil, A. Imam, N. F. Isa, M. A. Gondal, and M. A. Al-Osta, *Mater. Today Commun.*, 2023, **36**, 106409.
6 Y. Chen, Y. Lu, C. Lin, Y. Tian, C. J. Gao, L. Dong and C. Shan, *J. Mater. Chem. C*, 2018, **6**, 5727-5732.
7 M. Wei, K. Yao, Y. Liu, C. Yang, X. Zang, and L. Lin, *Small*, 2017, **13**, 1701328.
8 R. Rao, C. L. Pint, A. E. Islam, R. S. Weatherup, S. Hofmann, E. R. Meshot, F. Wu, C. Zhou, N. Dee, P. B. Amama, J. C.-Nuñez, W. Shi, D. L. Plata, E. S. Penev, B. I. Yakobson, P. B. Balbuena, C. Bichara, D. N. Futaba, S. Noda, H. Shin, K. S. Kim, B. Simard, F. Mirri, M. Pasquali, F. Fornasiero, E. I. Kauppinen, M. Arnold, B. A. Cola, P. Nikolaev, S. Arepalli, H. Cheng, D. N. Zakharov, E. A. Stach, J. Zhang, F. Wei, M. Terrones, D. B. Geohegan, B. Maruyama, S. Maruyama, Y. Li, W. W. Adams, and A. J. Hart, *ACS nano*, 2018, **12**, 11756-11784.
9 A. F. Zhou, R. Velázquez, X. Wang, and P. X. Feng, ACS Appl. Mater. Inter., 2019, **11**, 38068-38074.
10 P. Neumann, I. Jakobi, F. Dolde, C. Burk, R. Reuter, G. Waldherr, J. Honert, T. Wolf, A. Brunner, J. H. Shim, D. Suter, H. Sumiya, J. Isoya and J. Wrachtrup, *Nano Lett.*, 2013, 13, 2738-2742.
11 C. Bradac, W. Gao, J. Forneris, M. E. Trusheim and I. Aharonovich, *Nat. Commun.*, 2019, **10**, 5625.

12 B. C. Rose, D. Huang, Z. H. Zhang, P. Stevenson, A. M. Tyryshkin, S. Sangtawesin, S. Srinivasan1, L. Loudin, M. L. Markham, A. M. Edmonds, D. J. Twitchen, S. A. Lyon and N. P. De Leon, *Science*, 2018, **361** 60-63.

13 F. Dolde, I. Jakobi, B. Naydenov, N. Zhao, S. Pezzagna, C. Trautmann, J. Meijer, P. Neumann, F. Jelezko and J. Wrachtrup, *Nat. Phys.*, 2013, **9**, 139-143.

14 P. Sittimart, S. Ohmagari, H. Umezawa, H. Kato, K. Ishiji and T. Yoshitake, *Adv. Opt. Mater.*, 2023, **11**, 2203006.

15 F. M. Hrubesch, G. Braunbeck, M. Stutzmann, F. Reinhard, and M. S. Brandt, *Phys. Rev. Lett.*, 2017, **118**, 037601.

16 P. Siyushev, M. Nesladek, E. Bourgeois, M. Gulka, J. Hruby, T. Yamamoto, M. Trupke, T. Teraji, J. Isoyaand F. J. Agio, *Science*, 2019, **363**, 728-731.

17 E. Bourgeois, M. Gulka and M. Nesladek, *Adv. Opt. Mater.*, 2020, **8**, 1902132.

18 C. L. Smallwood, R. Ulbricht, M. W. Day, T. Schröder, K. M. Bates, T. M. Autry, G. Diederich, E. Bielejec, M. E. Siemens and S. T. Cundiff, *Phys. Rev. Lett.*, 2021, **126**, 213601.

19 L. Ondic, M. Varga, K. Hruška, J. Fait and P. Kapusta, *ACS nano*, **2017**, 11, 2972-2981.

20 M. A. Lobaev, A. M. Gorbachev, D. B. Radishev, A. L. Vikharev, S. A. Bogdanov, V. A. Isaev and M. N. Drozdov, *J. Mater. Chem. C*, 2021, **9**, 9229-9235.

21 B. Yang, J. Li, L. Guo, N. Huang, L. Liu, Z. Zhai, W. Long and X. Jiang, *CrystEngComm*, 2018, **20**, 1158-1167.

22 J. Lu, B. Yang, B. Yu, H. Li, N. Huang, L. Liu and X. Jiang, *Adv. Opt. Mater.*, 2021, **9**, 2101427.

23 B. Yang, B. Yu, H. Li, N. Huang, L. Liu, and X. Jiang, *Carbon*, 2020, **156**, 242-252.

24 B. Yu, B. Yang, H. Li, J. Lu, N. Huang, L. Liu and X. Jiang, *Appl. Surf. Sci.*, 2021, **552**, 149475.

25 P. E. Viljoen, E. S. Lambers and P. H. Holloway, *J. Vac. Sci. Technol. B*, 1994, **12**, 2997-3005.

26 S. Osswald, G. Yushin, V. Mochalin, S. O. Kucheyev and Y. Gogotsi, *J. Am. Chem. Soc.*, 2006, **128**, 11635-11642.

27 A. C. Ferrari and J. Robertson, *Phys. Rev. B*, 2001, **63**, 121405.

28 X. Jiang, C. P. Klages, R. Zachai, M. Hartweg and H. J. Füsser, *Appl. Phys. Lett.*, 1993, **62**, 3438-3440.

29 A. BenMoussa, A. Soltani, K. Haenen, U. Kroth, V. Mortet, H. A. Barkad, D. Bolsee, C. Hermans, M. Richter and J. C. De Jaeger, *Semicond. Sci. Tech.*, 2008, **23**, 035026.

30 A. Dietrich, K. D. Jahnke, J. M. Binder, T. Teraji, J. Isoya, L. J. Rogers and F. Jelezko, *New J. Phys.*, 2014, **16**, 113019.

31 S. Choi, V. N. Agafonov, V. A. Davydov and T. Plakhotnik, *ACS Photonics*, 2019, **6**, 1387-1392. View Article Online DOI: 10.1039/D4TC02335H

32 B. Andrey, R. Victor, S. Vadim, K. Andrey, V. Igor, K. Alexander, T. Nikolay, K. Vladimir, N. Sergei, K. Roman and S. Vladimir, *Phys. Status Solidi A*, 2015, **212**, 2525-2532.

33 C. Schreyvogel, M. Wolfer, H. Kato, M. Schreck and C. E. Nebel, *Sci. Rep.*, 2014, **4**, 3634.

34 Y. Wang, J. Su, Z. Lin, J. Zhang, J. Chang and Y. Hao, J. *Mater. Chem. C*, 2022, **10**, 13395-13436.

35 G. Simone, M. J. Dyson, S. C. Meskers, R. A. Janssen and G. H. Gelinck, *Adv. Funct. Mater.*, 2020, **30**, 1904205.

36 N. Youngblood, C. Chen, S. J. Koester and M. Li, *Nature Photon.*, 2015, **9**, 247-252.

37 Y. Sasama, T. Kageura, M. Imura, K. Watanabe, T. Taniguchi, T. Uchihashi and Y. Takahide, *Nat. Electron.*, 2022, **5**, 37-44.

38 J. Raymakers, K. Haenen and W. Maes, *J. Mater. Chem. C*, 2019, **7**, 10134-10165.

39 T. Murooka, M. Shiigai, Y. Hironaka, T. Tsuji, B. Yang, T. M. Hoang, K. Suda, K. Mizuno, H. Kato, T. Makino, M. Ogura, S. Yamasaki, M. Hatano and T. Iwasaki, *Appl. Phys. Lett.*, 2021, **118**, 253502.

40 C. Hepp, T. Müller, V. Waselowski, J. N. Becker, B. Pingault, H. Sternschulte, D. Steinmüller-Nethl, A. Gali, J. R. Maze, M. Atatüre and C. Becher, *Phys. Rev. Lett.*, 2014, **112**, 036405.

41 C. Lin, Y. Lu, X. Yang, Y. Tian, C. Gao, J. Sun, L. Dong, F. Zhong, W. Hu and C. Shan, *Adv. Opt. Mater.*, 2018, **6**, 1800068.

42 Z. Liu, F. Li, S. Li, C. Hu, W. Wang, F. Wang, F. Lin and H. Wang, *Sci. Rep.*, 2015, **5**, 14420..

43 C. Lin, Y. Lu, Y. Tian, C. Gao, M. Fan, X. Yang, L. Dong and C. Shan, *Opt. Express*, 2019, **27**, 29962-29971.

44 J. Chen and N. G. Park, *Adv. Mater.*, 2019, **31**, 1803019.

45 Z. Fan, H. Fan, L. Yang, P. Li, Z. Lu, G Tian, Z. Huang, Z. Li, J. Yao, Q. Luo, C. Chen, D. Chen, Z. Yan, M. Zeng, X. Lu, X. Gao and J.M. Liu, *J. Mater. Chem. C*, 2017, **5**, 7317-7327.

46 Z. C. Liu, F. N. Li, W. Wang, J. W. Zhang, F. Lin and H. X. Wang, *MRS Adv.*, 2016, **1**, 1099-1104.

47 X. Shi, Z. Yang, S. Yin, and H. Zeng, *Mater. Technol.*, 2016, **31**, 544-547.

48 X. Guo, B. Yang, J. Lu, H. Li, N. Huang, L. Liu and X. Jiang, *J. Mater. Chem. C*, 2022, **10**, 9334-9343.

View Article Online
DOI: 10.1039/D4TC02335H

Data Availability Statement

The data supporting this article have been included as part of the Supplementary Information.